

Magnetic-field annihilation and island formation in electron-scale current sheet in Earth's magnetotail

Hiroshi Hasegawa (✉ hase@stp.isas.jaxa.jp)

Institute of Space and Astronautical Science, JAXA <https://orcid.org/0000-0002-1172-021X>

Richard Denton

Department of Physics and Astronomy, Dartmouth College

Kevin Genestreti

Southwest Research Institute

Takuma Nakamura

Space Research Institute, Austrian Academy of Sciences

Tai Phan

Space Sciences Laboratory

Rumi Nakamura

Space Research Institute

Kyoung-Joo Hwang

Southwest Research Institute

Narges Ahmadi

Laboratory for Atmospheric and Space Physics, University of Colorado

Quanqi Shi

Shandong Provincial Key Laboratory of Optical Astronomy and Solar-Terrestrial Environment, Institute of Space Science, Shandong University, Weihai, Shandong

Michael Hesse

Space Plasma Physics Group, University of Bergen

James Burch

Southwest Research Institute <https://orcid.org/0000-0003-0452-8403>

James Webster

Rice University

Roy Torbert

University of New Hampshire <https://orcid.org/0000-0001-7188-8690>

Barbara Giles

NASA Goddard Space Flight Center

Daniel Gershman

NASA Goddard Space Flight Center

Christopher Russell

Department of Earth, Planetary and Space Sciences, University of California, Los Angeles

Robert Strangeway

Institute of Geophysics and Planetary Physics, UCLA

P.-A. Lindqvist

Royal Institute of Technology <https://orcid.org/0000-0001-5617-9765>

Yuri Khotyaintsev

Swedish Institute of Space Physics <https://orcid.org/0000-0001-5550-3113>

Robert Ergun

University of Colorado, Boulder

Yoshifumi Saito

JAXA

Article

Keywords: magnetic-to-particle energy conversion, electron-scale diffusion region, EDR, magnetic-field annihilation, island formation

Posted Date: July 30th, 2020

DOI: <https://doi.org/10.21203/rs.3.rs-40743/v1>

License:   This work is licensed under a Creative Commons Attribution 4.0 International License.

[Read Full License](#)

1 **Magnetic-field annihilation and island formation in electron-scale current sheet in**
2 **Earth's magnetotail**

3 **H. Hasegawa^{1*}, R. E. Denton², K. J. Genestreti³, T. K. M. Nakamura⁴, T. D. Phan⁵, R.**
4 **Nakamura⁴, K.-J. Hwang⁶, N. Ahmadi⁷, Q. Q. Shi⁸, M. Hesse⁹, J. L. Burch⁶, J. M.**
5 **Webster⁶, R. B. Torbert^{10,3}, B. L. Giles¹¹, D. J. Gershman¹¹, C. T. Russell¹², R. J.**
6 **Strangeway¹², P.-A. Lindqvist¹³, Y. V. Khotyaintsev¹⁴, R. E. Ergun¹⁵, and Y. Saito¹**

7 ¹Institute of Space and Astronautical Science, Japan Aerospace Exploration Agency,
8 Sagamihara, Japan.

9 ²Department of Physics and Astronomy, Dartmouth College, Hanover, NH, USA.

10 ³Southwest Research Institute, Durham, NH, USA.

11 ⁴Space Research Institute, Austrian Academy of Sciences, Graz, Austria.

12 ⁵Space Sciences Laboratory, University of California, Berkeley, CA, USA.

13 ⁶Southwest Research Institute, San Antonio, TX, USA.

14 ⁷Laboratory for Atmospheric and Space Physics, University of Colorado, Boulder, CO, USA.

15 ⁸Shandong Provincial Key Laboratory of Optical Astronomy and Solar-Terrestrial
16 Environment, Institute of Space Sciences, Shandong University, Weihai, China.

17 ⁹Space Plasma Physics Group, University of Bergen, Bergen, Norway.

18 ¹⁰Physics Department, University of New Hampshire, Durham, NH, USA.

19 ¹¹NASA Goddard Space Flight Center, Greenbelt, MD, USA.

20 ¹²Department of Earth, Planetary, and Space Sciences, University of California, Los Angeles,
21 CA, USA.

22 ¹³Royal Institute of Technology, Stockholm, Sweden.

23 ¹⁴Swedish Institute of Space Physics, Uppsala, Sweden.

24 ¹⁵Department of Astrophysical and Planetary Sciences, University of Colorado, Boulder, CO,
25 USA.

26 *e-mail: hase@stp.isas.jaxa.jp

27 Summary

28 **Establishing the mechanism of magnetic-to-particle energy conversion through magnetic**
29 **reconnection in current sheets¹ is the key to understanding the impact of fast release of**
30 **magnetic energy in many space and astrophysical plasma systems, such as during**
31 **magnetospheric substorms^{2,3}. It is generally believed that an electron-scale diffusion**
32 **region (EDR), where a magnetic-to-electron energy conversion occurs, has an X-type**
33 **magnetic-field geometry⁴ around which the energy of anti-parallel magnetic fields**
34 **injected is mostly converted to the bulk-flow energy of electrons by magnetic tension of**
35 **reconnected field-lines^{5,6}. However, it is at present unknown exactly how this energy**
36 **conversion occurs in EDRs, because there has been no observational method to fully**
37 **address this problem. Here we present state-of-the-art analysis of multi-spacecraft**
38 **observations in Earth's magnetotail of an electron-scale current sheet, which**
39 **demonstrates that contrary to the standard model of reconnection with an X-type EDR**
40 **geometry, the fast energy conversion in the detected EDR was caused mostly by magnetic-**
41 **field annihilation, rather than reconnection. Furthermore, we detected a magnetic island**
42 **forming in the EDR itself, implying that the EDR had an elongated shape ideal for island**
43 **generation⁷ and magnetic-field annihilation. The experimental discovery of the**
44 **annihilation-dominated EDR reveals a new form of energy conversion in the reconnection**
45 **process that can occur when the EDR has evolved from the X-type to planar geometry.**

46 Main text

47 Magnetic reconnection in Earth's magnetotail is fast, with an inflow plasma speed of ~ 0.1
48 times the inflow Alfvén speed, and has large-scale impacts, for example, on explosive release
49 of magnetic energy during magnetospheric substorms^{2,3}. Magnetotail reconnection occurs
50 under such simple boundary conditions that on the two sides of the current sheet the magnetic
51 fields are approximately oppositely-directed with a comparable intensity, and plasmas are
52 laminar with similar densities and temperatures. Such nearly anti-parallel and symmetric
53 reconnection is ideal for studying intrinsic properties of reconnection in collisionless plasmas.

54 In the standard model of reconnection, the EDR where both ions and electrons violate the
55 'frozen-in condition' and a magnetic-to-electron energy conversion occurs is localised with an
56 X-type magnetic-field geometry⁴ (Fig. 1a). It is generally accepted that in such EDRs most of
57 the energy of anti-parallel magnetic fields injected by the inflow is partitioned to the bulk-flow
58 energy^{5,6} of electrons ejected into the regions downstream of the EDR, called the exhausts, by
59 magnetic tension (Lorentz force) of reconnected field-lines. Numerical simulations⁷ suggest
60 that the EDR may be elongated to a planar geometry (Fig. 1b) and such a spatially extended
61 EDR can be a site ideal for the generation and growth of small-scale magnetic islands (Fig.
62 1c,d). However, evidence for islands forming in the EDR itself has so far been lacking.
63 Moreover, it is unknown exactly how the energy conversion occurs in observed EDRs. This is
64 not only because unambiguous identification of EDR structures in space requires high-
65 spatiotemporal-resolution plasma measurements, but also because there has been no data-
66 analysis method to distinguish whether the magnetic field injected into the EDR is reconnected
67 or annihilated.

68 Here we present in-depth analysis of the fortuitous multi-spacecraft observations of a
69 magnetotail EDR⁸, providing direct evidence for a magnetic island forming in an elongated
70 electron-scale current sheet (ECS). Fast four-point measurements of electromagnetic fields and
71 plasmas by the Magnetospheric Multiscale (MMS) mission⁹, combined with novel data-
72 analysis techniques, demonstrate that fast magnetic-to-particle energy conversion in the
73 detected ECS was dominated by magnetic-field annihilation, rather than reconnection.

74 In Fig. 2a–d, we show the context of the reconnecting current sheet observed by the MMS
 75 2 spacecraft on 10 August 2017 at 12:17:40–12:19:40 UT, when MMS was fully embedded in
 76 the hot magnetotail plasma sheet⁸ at geocentric solar magnetospheric (GSM) coordinates of
 77 (−15.2, 4.6, 3.1) in units of Earth radii and a weak substorm occurred with a peak Auroral
 78 Electrojet index¹⁰ of ~200 nT. The current sheet at 12:18:30 UT is characterized by a reversal
 79 from anti-sunward to sunward ion flows (negative to positive v_{ix} change in Fig. 2b), crossing
 80 from its southern to northern side (negative to positive B_x change in Fig. 2a). The ion flow
 81 speeds around the start and end of the interval are comparable to the ion Alfvén speed $V_{iA} =$
 82 $B/(\mu_0\rho)^{1/2} \approx 850 \text{ km s}^{-1}$ based on the magnetic field intensity $B \approx 15 \text{ nT}$ and proton number
 83 density of 0.15 cm^{-3} , where μ_0 is the vacuum permeability and ρ is plasma mass density. A
 84 fast downward electron flow ($v_{ey} \approx -10 \text{ Mm s}^{-1}$ in Fig. 2c) and a relatively slow duskward
 85 ion flow with no enhancement at the current sheet show that its electric current was supported
 86 by electrons. These features indicate that MMS crossed an ECS embedded inside a region of
 87 large-scale reconnection when traversing from its anti-sunward exhaust to sunward exhaust.
 88 Earlier studies of this current sheet^{8,11} reported established signatures of EDRs^{4,9}, including
 89 oppositely-directed electron jets with a speed exceeding V_{iA} (Fig. 2c), crescent-shaped electron
 90 velocity distributions and magnetic-to-particle energy conversion.

91 We investigate the ECS structure in detail by use of two sophisticated data-analysis
 92 techniques (Methods) that can reconstruct multi-dimensional magnetic field structures in
 93 regions around the spacecraft from in situ measurements of the magnetic field and plasma bulk
 94 parameters (density, velocity, and temperature for ions and electrons). One is a single-
 95 spacecraft method based on electron-magnetohydrodynamics (EMHD) equations that can
 96 recover quasi-steady, two-dimensional (2-D) magnetic, electrostatic, and electron-velocity
 97 fields around the path of the observing spacecraft, hereafter called the EMHD reconstruction¹².
 98 The other is a multi-spacecraft method based on polynomial (second-order Taylor) expansion
 99 of the magnetic field that can recover three-dimensional (3-D) magnetic field using
 100 instantaneous measurements by the four spacecraft of the magnetic field and particle current
 101 density, called the polynomial reconstruction¹³.

102 Figure 2e–k shows the magnetic field and plasma data from MMS used as input for the two
 103 reconstruction techniques, in a current-sheet (‘LMN’) coordinate system (Methods): the
 104 current-sheet normal points along N (roughly northward in the magnetotail), the reconnecting
 105 anti-parallel magnetic field component is along L (roughly sunward), and $M = N \times L$ is along
 106 the ‘X-line’ direction (roughly duskward). A weak guide field ($\sim 2 \text{ nT}$)⁸, the component (B_M)
 107 along the X-line of the magnetic field external to the entire larger-scale current sheet or, in this
 108 case, at the centre of the ECS (Fig. 2f), confirms that reconnection occurred under nearly anti-
 109 parallel magnetic-field conditions. Negative to positive variations of B_N (Fig. 2g) is consistent
 110 with MMS moving from the anti-sunward to sunward side of the reconnection site; the X-line
 111 was moving anti-sunward (Methods). The assumptions of constant density and constant and
 112 isotropic electron temperature made in the EMHD reconstruction are approximately satisfied
 113 for an intense current-density interval at 12:18:32.1–12:18:34.0 UT (Fig. 2i,k), to which the
 114 method is applied. The spacecraft separation $\sim 18 \text{ km}$ was comparable to the electron inertial
 115 length ($d_e \sim 14 \text{ km}$), allowing us to determine the ECS structure.

116 Both the EMHD and polynomial reconstruction results (Fig. 3a–d, f–i) clearly show that an
 117 electron-scale magnetic island was forming and growing in the ECS with a thickness of about
 118 one d_e . Figure 3a-d suggests that over a $\sim 0.4 \text{ s}$ interval of 12:18:32.6–12:18:33.0 UT, during
 119 which the current sheet was crossed in the order of MMS 1, MMS 3, MMS 4, and MMS 2 (Fig.
 120 2e), both the length (along L) and width (along N) of the island grew. An entirely consistent
 121 feature is seen in Fig. 3f-i. Furthermore, the energy-conversion rate $\mathbf{j} \cdot \mathbf{E}' = \mathbf{j}_p \cdot (\mathbf{E} +$

122 $\mathbf{v}_e \times \mathbf{B}$)¹⁴ (Fig. 3e), where the particle current density is $\mathbf{j}_p = en_e(\mathbf{v}_i - \mathbf{v}_e)$ with the
 123 elementary charge of e , \mathbf{E} the electric field measured in the spacecraft frame and \mathbf{B} the
 124 magnetic field, is strongly positive around an X-point closer to the centre of the reconstruction
 125 domain. Its magnitude ($\sim 0.5 \text{ nW m}^{-3}$) is comparable to an expected value ($\sim 0.2 \text{ nW m}^{-3}$)
 126 based on the current density $\sim 150 \text{ nA m}^{-2}$ (Fig. 2h) and reconnection electric field ~ 1.3
 127 mV m^{-1} expected for $B \approx 15 \text{ nT}$ and inflow ion speed of $\sim 0.1V_{iA} \approx 85 \text{ km s}^{-1}$ (Fig. 2b). We
 128 thus conclude that reconnection at the X-point was ongoing. Note that the active X-point was
 129 captured inside the MMS tetrahedron during the ECS crossing (Fig. 3a–d,g,h), reinforcing the
 130 conclusions based on the reconstruction results. Our multi-spacecraft analysis also shows that
 131 the encountered ECS was elongated in the exhaust (\mathbf{L}) direction (Methods).

132 In order to reveal how fast the magnetic island was growing, we calculated the amount of
 133 magnetic flux per unit length along \mathbf{M} embedded between the reconstructed X- and O-points
 134 closer to the centre of the reconstruction domain. Consistent with the island growth, the flux
 135 increases with time (Fig. 4a) and the measured component (E_M) along \mathbf{M} of the electric field
 136 appears to vary in space and time (Fig. 4c). However, the estimated reconnection electric fields
 137 (Fig. 4b) are about one order of magnitude smaller than the measured E_M that is comparable to
 138 the expected value of $\sim 1.3 \text{ mV m}^{-1}$. This result, surprisingly, suggests that the in-plane
 139 magnetic field injected into the ECS was mostly annihilated, rather than reconnected, at the
 140 time and portion of the ECS observed by MMS.

141 Another observational signature consistent with the annihilation-dominated EDR is the
 142 electron outflow speed ($\sim 3,000 \text{ km s}^{-1}$) (Fig. 2j and Extended Data Fig. 2b) much lower than
 143 the electron Alfvén speed ($V_{eA} \approx 17 \text{ Mm s}^{-1}$) based on $B_L = 7 \text{ nT}$ outside of the ECS (Fig.
 144 2e) and $n_e = 0.15 \text{ cm}^{-3}$ (Fig. 2i). It is possible that magnetic tension resulting under a low
 145 reconnection rate (E_{Ree} of order 0.1 mV m^{-1}) (Fig. 4b) was not strong enough to accelerate
 146 electrons, injected into the ECS at a high rate (equivalent to $E_{\text{str},M} = 1 - 2 \text{ mV m}^{-1}$) (Fig. 4c),
 147 to a speed comparable to V_{eA} .

148 Is fast annihilation of the magnetic field as detected by MMS physically possible in an
 149 ECS? For quasi-steady 2-D reconnection in collisionless plasmas, electron unmagnetisation
 150 (violation of the electron frozen-in condition) at the X-line occurs when off-diagonal terms of
 151 the electron pressure tensor are significant¹⁵. Consistently, non-gyrotropic electron velocity
 152 distributions as a manifestation of electron unmagnetisation have been observed in the present⁸
 153 as well as other EDRs^{4,9}, and earlier studies demonstrated that they can quantitatively account
 154 for the electric field (E_M) of fast reconnection as observed^{16,17}. We derive a diffusion equation
 155 for B_L (equation (4) in Methods),

$$156 \quad \frac{\partial B_L}{\partial t} \approx r_{ge} V_\infty \frac{\partial^2 B_L}{\partial N^2}, \quad (1)$$

157 where r_{ge} is the gyroradius of thermal electrons and V_∞ is the electron inflow speed ($|v_{eN}|$)
 158 immediately outside of the EDR, that is applicable when the generalized Ohm's law has a term
 159 equivalent to the non-gyrotropic electron pressure tensor and the ECS is elongated in the
 160 exhaust direction. This equation is supported by a solution of the EMHD equations and is
 161 consistent with the observed magnetic-field annihilation (Methods). The fast annihilation is in
 162 stark contrast with the classic (resistive magnetohydrodynamics) model^{18,19} of reconnection in
 163 an elongated current sheet in which magnetic-field annihilation is negligibly small under
 164 magnetotail conditions. However, we do not exclude a likely possibility that at around the
 165 sunward and anti-sunward ends of the present ECS, where the magnetic field may have a Y-
 166 type geometry (Fig. 1b,c), the magnetic field was efficiently reconnected and ejected
 167 downstream, as observed for other magnetotail reconnection events²⁰.

168 The approximately planar ECS, electron-scale island forming in the EDR itself and
 169 annihilation-dominated energy conversion, detected in this study, all support the existence of
 170 an EDR elongated in the exhaust direction (Fig. 1c) that is favourable for the island generation⁷.
 171 The detection of an island forming in such an EDR suggests that MMS serendipitously
 172 encountered the very initial stage of the island growth, so that the growth rate may be low (Fig.
 173 4c). The present observations also suggest that magnetic island formation is an intrinsic process
 174 in the EDR of anti-parallel reconnection, supporting the conclusion from a kinetic simulation⁷,
 175 rather than other simulation studies that predicted that an island may form in ECSs only when
 176 the guide field is large²¹. Furthermore, the experimental discovery of magnetic-field
 177 annihilation in a reconnecting ECS provides the first direct confirmation that magnetic energy
 178 can be irreversibly dissipated through collisionless reconnection²². Magnetic island formation
 179 and magnetic-field annihilation are key ingredients for the generation^{23,24} and dissipation,
 180 respectively, of plasma turbulent energy and could play a role in electron acceleration²⁵⁻²⁷.
 181 These aspects and the role played by magnetic-field annihilation in electron heating will need
 182 to be quantitatively assessed in the future, but our finding reveals a new form of magnetic-to-
 183 particle energy conversion in the reconnection process that can occur when the EDR has
 184 evolved from the X-type to planar geometry.

185 **Data availability**

186 The entire MMS dataset is publicly available at <https://lasp.colorado.edu/mms/sdc/public/>.

187 **Online content**

188 Methods, along with any additional Extended Data figures and references and Source Data, are
 189 available in the online version of the paper.

190 **References**

- 191 1. Yamada, M., Kulsrud, R. & Ji, H. Magnetic reconnection. *Rev. Mod. Phys.*, **82**, 603–664
 192 (2010).
- 193 2. Angelopoulos, V., McFadden, J. P., Larson, D. et al. Tail reconnection triggering substorm
 194 onset. *Science*, **321**, 931–935 (2008).
- 195 3. Nagai, T., Shinohara, I., Fujimoto, M., Matsuoka, A., Saito, Y., & Mukai, T. Construction
 196 of magnetic reconnection in the near-Earth magnetotail with Geotail. *J. Geophys. Res.*, **116**,
 197 A04222 (2011).
- 198 4. Torbert, R. B., Burch, J. L., Phan, T. D. et al. Electron-scale dynamics of the diffusion
 199 region during symmetric magnetic reconnection in space. *Science*, **362**, 1391–1395 (2018).
- 200 5. Cassak, P. A. & Shay M. A. Scaling of asymmetric magnetic reconnection: General theory
 201 and collisional simulations, *Phys. Plasmas*, **14**, 102114 (2007).
- 202 6. Shay, M. A., Drake, J. F. & Swisdak, M. Two-scale structure of the electron dissipation
 203 region during collisionless magnetic reconnection. *Phys. Rev. Lett.*, **99**, 155002 (2007).
- 204 7. Daughton, W., Scudder, J. & Karimabadi, H. Fully kinetic simulations of undriven
 205 magnetic reconnection with open boundary conditions. *Phys. Plasmas*, **13**, 072101 (2006).
- 206 8. Zhou, M., Deng, X. H., Zhong, Z. H. et al. Observations of an electron diffusion region in
 207 symmetric reconnection with weak guide field. *Astrophys. J.*, **870**, 34 (2019).
- 208 9. Burch, J. L., Torbert, R. B., Phan, T. D. et al. Electron-scale measurements of magnetic
 209 reconnection in space. *Science*, **352**, aaf2939 (2016).
- 210 10. Davis, T. N. & Sugiura, M. Auroral electrojet activity index *AE* and its universal time
 211 variations. *J. Geophys. Res.*, **71**, 785–801 (1966).

- 212 11. Li, X., Wang, R., Lu, Q. et al. Observation of nongyrotropic electron distribution across
 213 the electron diffusion region in the magnetotail reconnection. *Geophys. Res. Lett.*, **46**,
 214 14263–14273 (2019).
- 215 12. Sonnerup, B. U. Ö., Hasegawa, H., Denton, R. E. & Nakamura, T. K. M. Reconstruction
 216 of the electron diffusion region. *J. Geophys. Res. Space Physics*, **121**, 4279–4290 (2016).
- 217 13. Denton, R. E., Torbert, R. B., Hasegawa, H. et al. Polynomial reconstruction of the
 218 reconnection magnetic field observed by multiple spacecraft. *J. Geophys. Res. Space
 219 Physics*, **125**, e2019JA027481 (2020).
- 220 14. Zenitani, S., Hesse, M., Klimas, A. & Kuznetsova, M. New measure of the dissipation
 221 region in collisionless magnetic reconnection. *Phys. Rev. Lett.* **106**, 195003 (2011).
- 222 15. Hesse, M., Neukirch, T., Schindler, K., Kuznetsova, M. & Zenitani, S. The diffusion region
 223 in collisionless magnetic reconnection. *Space Sci. Rev.*, **160**, 3–23 (2011).
- 224 16. Nakamura, R., Genestreti, K. J., Nakamura, T. K. M. et al. Structure of the current sheet in
 225 the 11 July 2017 Electron Diffusion Region event. *J. Geophys. Res. Space Physics*, **124**,
 226 1173–1186 (2019).
- 227 17. Egedal, J., Ng, J., Le, A. et al. Pressure tensor elements breaking the frozen-in law during
 228 reconnection in Earth’s magnetotail. *Phys. Rev. Lett.*, **123**, 225101 (2019).
- 229 18. Parker, E. N. Sweet’s mechanism for merging magnetic fields in conducting fluids. *J.
 230 Geophys. Res.*, **62**, 509–520 (1957).
- 231 19. Sweet, P. A. in *Electromagnetic Phenomena in Cosmical Physics* (ed. Lehnert, B.)
 232 Cambridge, 123–134 (1958).
- 233 20. Nakamura, T. K. M., Genestreti, K. J., Liu, Y.-H. et al. Measurement of the magnetic
 234 reconnection rate in the Earth’s magnetotail. *J. Geophys. Res. Space Physics*, **123**, 9150–
 235 9168 (2018).
- 236 21. Drake, J. F., Swisdak, M., Schoeffler, K. M., Rogers, B. N. & Kobayashi, S. Formation of
 237 secondary islands during magnetic reconnection. *Geophys. Res. Lett.*, **33**, L13105 (2006).
- 238 22. Phan, T. D., Eastwood, J. P., Shay, M. A. et al. Electron magnetic reconnection without ion
 239 coupling in Earth’s turbulent magnetosheath. *Nature*, **557**, 202–206 (2018).
- 240 23. Daughton, W., Roytershteyn, V., Karimabadi, H. et al. Role of electron physics in the
 241 development of turbulent magnetic reconnection in collisionless plasmas. *Nat. Phys.*, **7**,
 242 539–542 (2011).
- 243 24. Franci, L., Cerri, S. S., Califano, F. et al. Magnetic reconnection as a driver for a sub-ion-
 244 scale cascade in plasma turbulence. *Astrophys. J. Lett.*, **850**, L16 (2017).
- 245 25. Drake, J. F., Swisdak, M., Che, H. & Shay, M. A. Electron acceleration from contracting
 246 magnetic islands during reconnection. *Nature*, **443**, 553–556 (2006).
- 247 26. Chen, L.-J., Bhattacharjee, A., Puhl-Quinn, P. A. et al. Observation of energetic electrons
 248 within magnetic islands. *Nat. Phys.*, **4**, 19–23 (2008).
- 249 27. Wang, R., Lu, Q., Du, A. & Wang, S. In situ observations of a secondary magnetic island
 250 in an ion diffusion region and associated energetic electrons. *Phys. Rev. Lett.*, **104**, 175003
 251 (2010).
- 252 28. Dunlop, M. W., Balogh, A., Glassmeier, K.-H. & Robert, P. Four-point Cluster application
 253 of magnetic field analysis tools: The Curlometer. *J. Geophys. Res.*, **107**, 1384 (2002).

254 Acknowledgments

255 We are grateful for the dedicated efforts of the MMS team. This work was supported by a
 256 NASA grant (80NSSC19K0254) and the Austrian Research Fund (FWF) P32175-N27. H.H.
 257 thanks W. Daughton for discussions.

258 **Author contributions**

259 H.H. and R.E.D. carried out the data analysis and interpretation, theoretical analysis and
 260 manuscript preparation. K.J.G., T.K.M.N., T.D.P., R.N., K.J.H., N.A., and J.M.W. contributed
 261 to the data interpretation and manuscript preparation. Q.Q.S. contributed to the data analysis
 262 and interpretation. M.H. contributed to the theoretical analysis. J.L.B. led the successful design
 263 and operation of the MMS mission and contributed to the data interpretation. R.B.T., P.A.L.,
 264 Y.V.K., and R.E.E. contributed to the development and operation of the electric-field
 265 experiments. B.L.G., D.J.G. and Y.S. contributed to the development and operation of and the
 266 interpretation of data from the Fast Plasma Investigation instruments. C.T.R. and R.J.S.
 267 contributed to the development and operation of the fluxgate magnetometers.

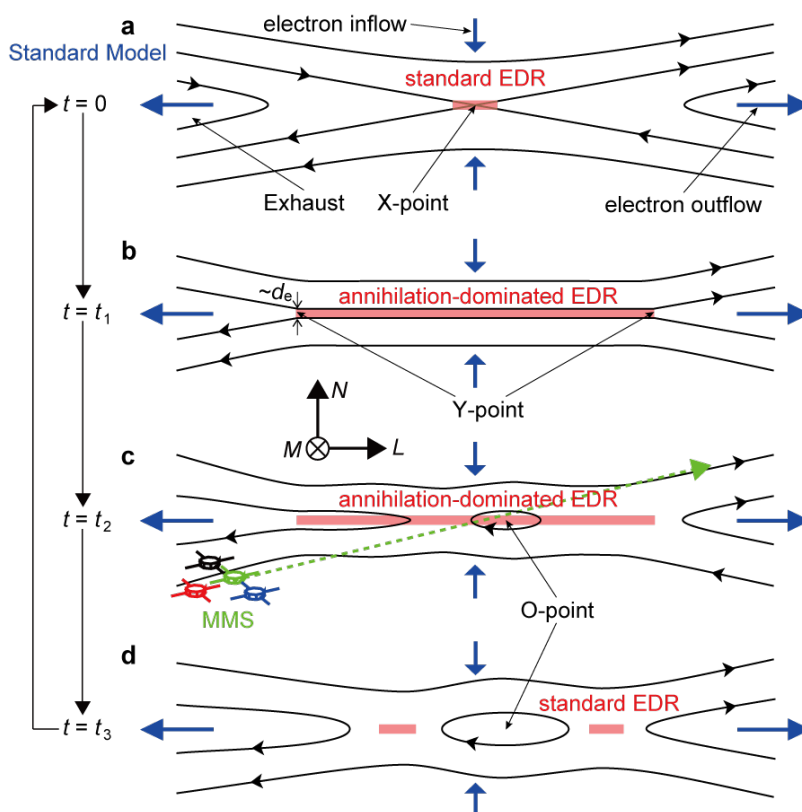
268 **Competing interests**

269 The authors declare no competing interests.

270 **Additional information**

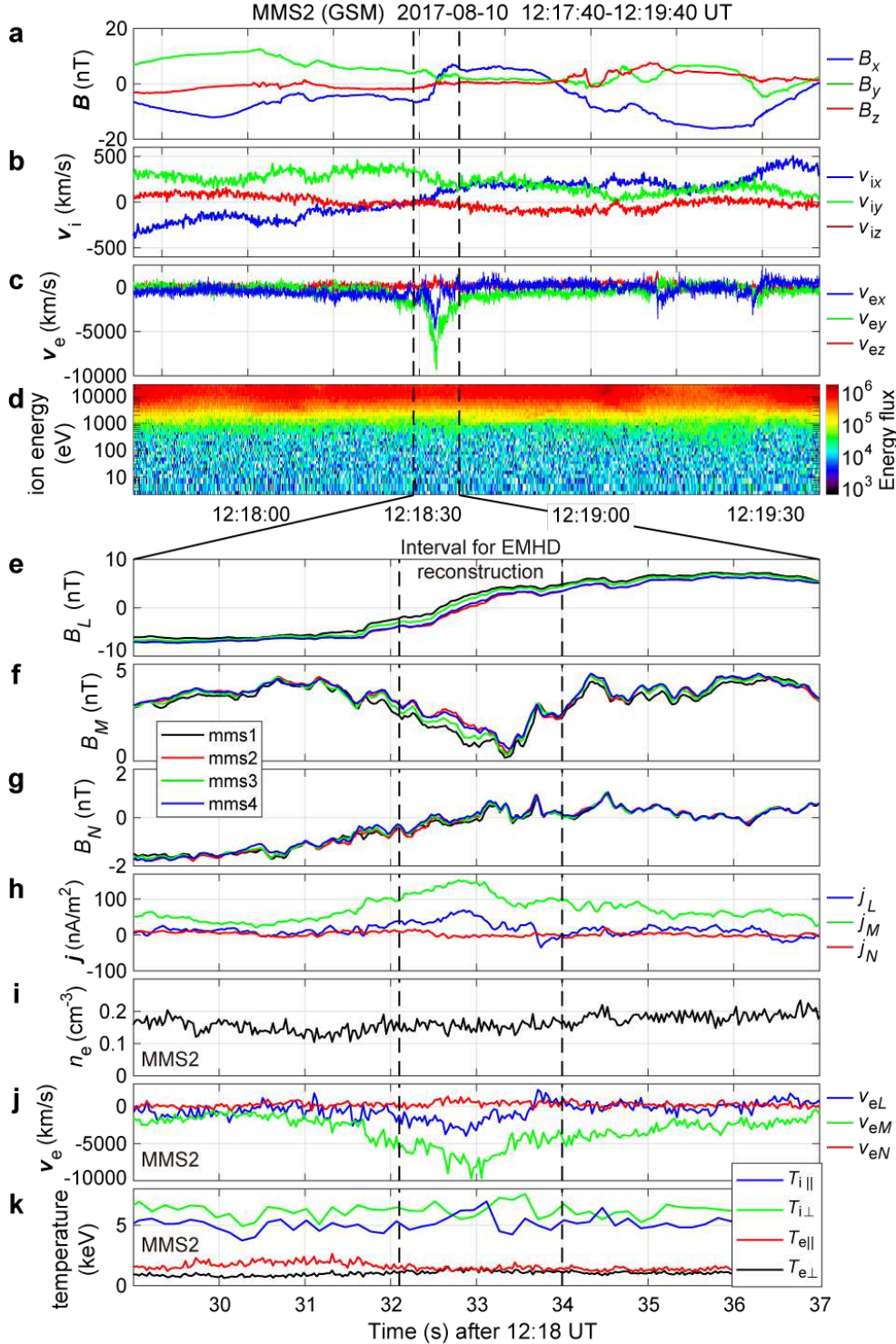
271 **Correspondence and requests for materials** should be addressed to H.H.

272



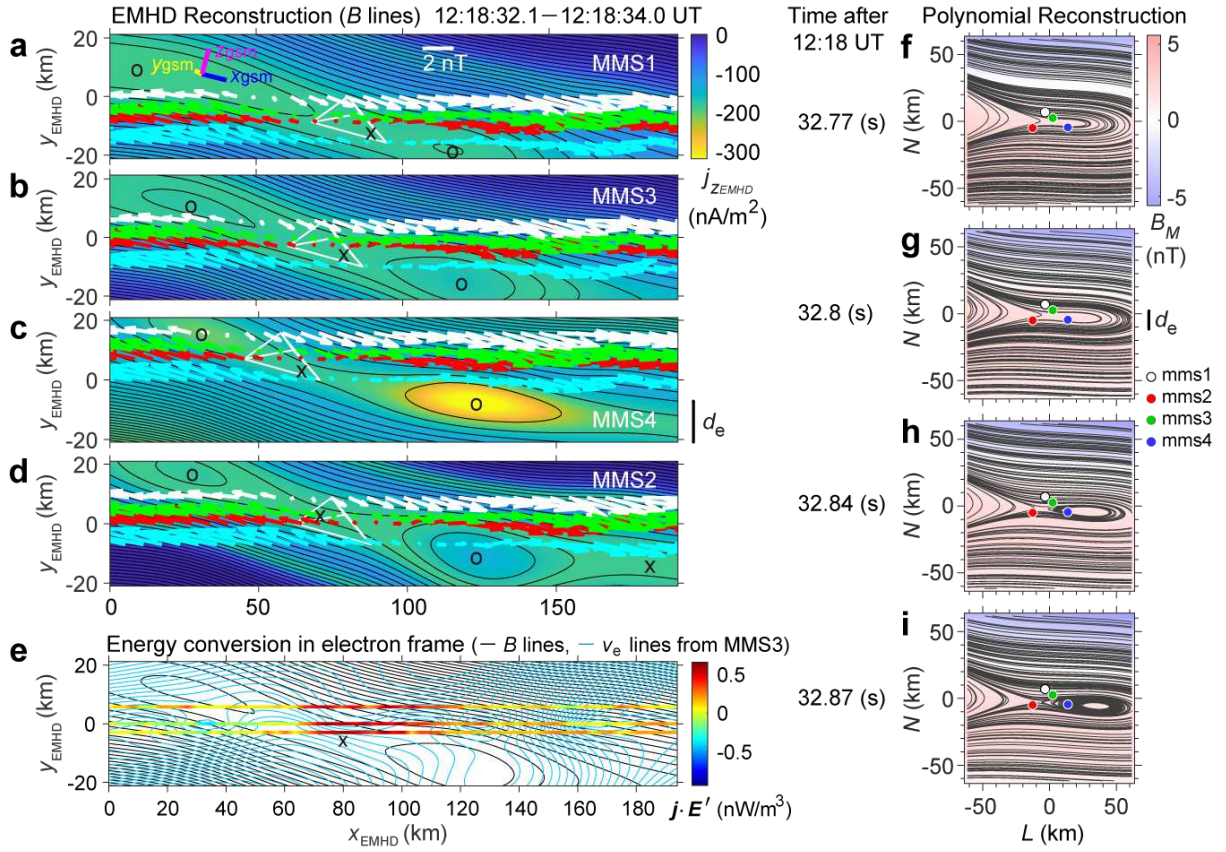
273

274 **Fig. 1 | Standard picture of the reconnection region and possible sequence of time**
 275 **evolution of the observed electron-scale current sheet. a,** Standard EDR with an X-type
 276 magnetic-field geometry where the magnetic-to-particle energy conversion is mostly due to
 277 reconnection⁴. **b,** EDR after elongation along L , as seen in simulation⁷, where the energy
 278 conversion may be mostly due to magnetic-field annihilation (Methods). **c,** Initial stage of the
 279 magnetic-island formation in the EDR, as observed by MMS. **d,** Possible later stage of the
 280 island growth in exhausts of the EDRs where the energy conversion is again dominated by
 281 reconnection.



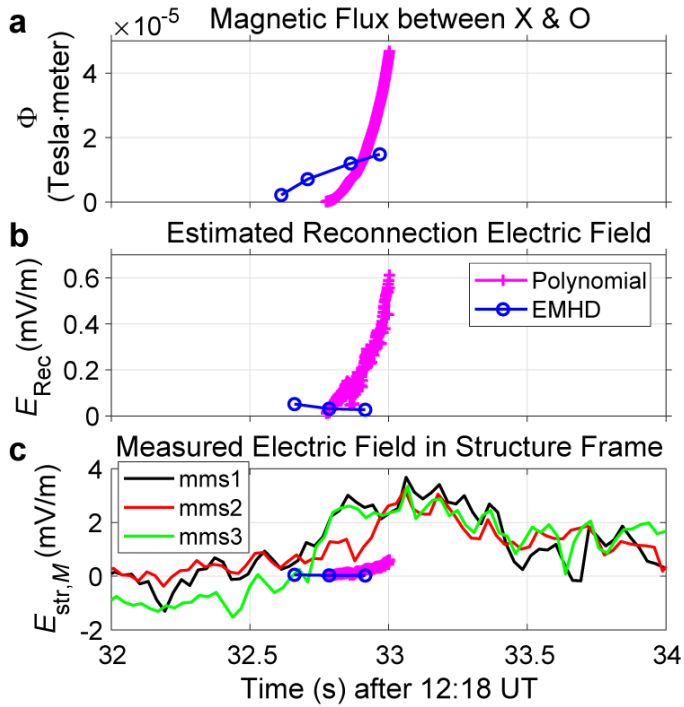
282
283
284
285
286
287
288
289
290
291
292

Fig. 2 | Overview of MMS observations of an ECS with both ion and electron reconnection jet signatures. **a–d**, GSM components of the magnetic field (**a**; B_x , B_y and B_z), ion velocity (**b**; v_{ix} , v_{iy} and v_{iz}), electron velocity (**c**; v_{ex} , v_{ey} and v_{ez}) and ion energy-time spectrogram of omni-directional differential energy flux (**d**; colour scale, in units of $\text{keV s}^{-1} \text{cm}^{-2} \text{sr}^{-1} \text{keV}^{-1}$) seen by MMS 2. **e–h**, Components in a common current-sheet (LMN) coordinate system of the magnetic field (**e–g**; B_L , B_M and B_N) from all four spacecraft (black, MMS 1; red, MMS 2; green, MMS 3; blue, MMS 4) and current density $\mathbf{j} = (\nabla \times \mathbf{B})/\mu_0$ ²⁸ (**h**; j_L , j_M and j_N). **i–k**, MMS 2 measurements of the electron density (**i**; n_e), electron velocity in LMN coordinates (**j**; v_{eL} , v_{eM} and v_{eN}), and ion and electron temperatures (**k**; T_i and T_e) in the directions parallel (\parallel) and perpendicular (\perp) to the local magnetic field.



293

294 **Fig. 3 | Magnetic fields recovered from the two reconstruction methods (Methods).** **a–d**,
 295 2-D magnetic fields from the EMHD reconstruction¹² using the data taken at 12:18:32.1–
 296 12:18:34.0 UT individually for each of the four spacecraft, shown in the order of current sheet
 297 crossing (MMS 1, **a**; MMS 3, **b**; MMS 4, **c**; then MMS 2, **d**; as seen in Fig. 2e). Black curves
 298 show the reconstructed magnetic field-lines, colours the out-of-plane component ($j_{z,EMHD}$) of
 299 the reconstructed current density, and arrows the projections onto the reconstruction (x_{EMHD} –
 300 y_{EMHD}) plane of the measured magnetic fields (white, MMS 1; red, MMS 2; green, MMS 3;
 301 cyan, MMS 4) along the paths of the four spacecraft. The bars near the upper-left corner of Fig.
 302 3a are the projections of the unit GSM axes (blue, \hat{x}_{GSM} ; yellow, \hat{y}_{GSM} ; magenta, \hat{z}_{GSM}). **e**,
 303 Magnetic field-lines (black curves) and electron streamlines (blue curves) reconstructed from
 304 the MMS 3 data, with $\mathbf{j} \cdot \mathbf{E}' = \mathbf{j}_p \cdot (\mathbf{E} + \mathbf{v}_e \times \mathbf{B})$ ¹⁴ measured along the paths of MMS 1, MMS
 305 2, and MMS 3 in colour. **f–i**, Projection onto the L – N plane of 3-D magnetic field-lines
 306 reconstructed using the polynomial reconstruction¹³ from instantaneous measurements (time
 307 after 12:18 UT: 32.77 s, **f**; 32.8 s, **g**; 32.84 s, **h**; 32.87 s, **i**) by the four spacecraft of \mathbf{B} and \mathbf{j}_p ,
 308 with reconstructed B_M in colour.



309
 310
 311
 312
 313
 314
 315
 316
 317

Fig. 4 | Reconnection electric fields, estimated from the EMHD and polynomial reconstructions, compared with the measured electric field. **a**, In-plane magnetic flux (Φ) embedded between the X- and O-points around the centre of the reconstruction domain as a function of time which is defined as that of the current sheet crossing ($B_L = 0$) for the EMHD reconstruction. **b**, Reconnection electric field ($E_{\text{Rec}} = \partial\Phi/\partial t$) estimated from the temporal rate of change in Φ . **c**, M component ($E_{\text{str},M}$) of the electric field from MMS 1, MMS 2, and MMS 3 that made reliable electric field measurements, transformed into the frame comoving with the structure (Methods), along with E_{Rec} .

318 **Methods**319 **Data handling.**

320 For this study, MMS burst-mode data from the following instrument suites were used:
 321 FIELDS²⁹, including the electric-field instruments^{30,31} and magnetometers³², and FPI (electron
 322 and ion plasma distributions and moments)³³. All data are from the standard level-2 data
 323 products, which are publicly available at the MMS Science Data Center
 324 (<https://lasp.colorado.edu/mms/sdc/public>).

325 **Current-sheet (LMN) coordinate system.**

326 The final LMN coordinate system used in this study, with $\mathbf{L} =$
 327 $(0.955, -0.298, -0.021)_{\text{GSM}}$, $\mathbf{M} = (0.296, 0.953, -0.059)_{\text{GSM}}$, and $\mathbf{N} =$
 328 $(0.038, 0.050, 0.998)_{\text{GSM}}$, was determined through optimization of the EMHD reconstruction
 329 results, as detailed below. A preliminary LMN coordinate system used as trial LMN axes in
 330 the reconstruction was determined by a hybrid method³⁴, which combines the Minimum
 331 Variance Analysis (MVA)³⁵ and Maximum Directional Derivative (MDD) method³⁶ of the
 332 magnetic field, applied to four-spacecraft measurements of the magnetic field at 12:18:31–
 333 12:18:36 UT. The resulting LMN axes are: $\mathbf{L}_p = (0.992, -0.127, -0.022)_{\text{GSM}}$, $\mathbf{M}_p =$
 334 $(0.127, 0.992, -0.003)_{\text{GSM}}$, and $\mathbf{N}_p = (0.022, -0.000, 1.000)_{\text{GSM}}$, which are not very
 335 different from the final axes. Results from the MDD method are presented in Extended Data
 336 Fig. 1, which shows that the current sheet was roughly planar locally (Extended Data Fig. 1f),
 337 satisfying the assumption underlying the MVA, and that the current-sheet normal was stably
 338 northward (Extended Data Fig. 1g).

340 **Frame velocity.**

341 The frame velocity comoving with the structure was estimated by a multi-spacecraft data-
 342 analysis technique known as the spatiotemporal difference (STD) method³⁷, applied to
 343 smoothed magnetic field data from the four spacecraft at 12:18:32.0–12:18:33.3 UT. The
 344 velocity component from the STD method along the minimum magnetic-gradient direction
 345 \mathbf{k}_{min} , which is often along \mathbf{M} (Extended Data Fig. 1i), is usually unreliable³⁸ and was not used.
 346 The resulting velocity is $\mathbf{V}_{\text{STD}} = -100\mathbf{L}_p - 28\mathbf{N}_p \text{ km s}^{-1}$, consistent with an anti-sunward
 347 moving EDR and south-to-north crossing of the ECS. The normal velocity roughly agrees well
 348 with that (-35 km s^{-1}) estimated by multi-spacecraft timing analysis⁸. The L -component
 349 dominated motion of the structure, combined with the approximately planar geometry of the
 350 ECS (Extended Data Fig. 1f), indicates that the ECS was elongated in the exhaust direction
 351 (Fig. 1b,c). The L and N components of the final structure velocity $\mathbf{V}_{\text{str}} =$
 352 $(-30, 237, -40)_{\text{GSM}} \text{ km s}^{-1}$, used in the EMHD reconstruction, are the projections along \mathbf{L}
 353 and \mathbf{N} of \mathbf{V}_{STD} and the M component ($V_{\text{str},M}$) is that of the mean ion velocity for the
 354 reconstruction interval, so that the electric current is supported mostly by electrons in the
 355 structure frame. The electric field transformed into the structure frame is $\mathbf{E}_{\text{str}} = \mathbf{E} + \mathbf{V}_{\text{str}} \times \mathbf{B}$.

357 **EMHD reconstruction.**

358 The EMHD reconstruction¹² recovers 2-D magnetic, electrostatic, and electron-velocity
 359 fields in the reconstruction ($x_{\text{EMHD}}-y_{\text{EMHD}}$) plane around the path ($y_{\text{EMHD}} = 0$) of a single
 360 spacecraft from the magnetic field and ion and electron moments data taken by the spacecraft,
 361 once a proper LMN coordinate system and frame velocity are defined. The underlying
 362 assumptions are that the structure is time-independent in its rest frame ($\partial/\partial t = 0$) and 2-D
 363 ($\partial/\partial z_{\text{EMHD}} = 0$) and has a constant frame velocity \mathbf{V}_{str} (straight spacecraft path), electron-
 364 inertia terms and ion dynamics can be neglected, and the electron density n_e is constant in
 365 space and time. The x_{EMHD} axis is defined to be anti-parallel to the projection of \mathbf{V}_{str} onto the

367 plane perpendicular to $\hat{\mathbf{z}}_{\text{EMHD}} = -\mathbf{M}$, and $\hat{\mathbf{y}}_{\text{EMHD}} = \hat{\mathbf{z}}_{\text{EMHD}} \times \hat{\mathbf{x}}_{\text{EMHD}}$. The generalized Ohm's
 368 law (electron momentum equation) used in the reconstruction is thus

$$369 \quad \mathbf{E} = -\mathbf{v}_e \times \mathbf{B} - \frac{\nabla \cdot \mathbf{P}}{n_e e} \quad (1)$$

370 with $\nabla \cdot \mathbf{P} = \nabla \tilde{p} + \hat{\mathbf{z}}_{\text{EMHD}} f(x_{\text{EMHD}}, y_{\text{EMHD}})$ where \mathbf{P} is the electron pressure tensor, $\tilde{p} =$
 371 $n_e k_B T_e$ is the part of isotropic electron pressure, which is assumed to be constant and thus
 372 $\nabla \tilde{p} = 0$. Here k_B is the Boltzmann constant. It has been shown that the term

$$373 \quad f(x_{\text{EMHD}}, y_{\text{EMHD}}) = f(L, N) = n_e \sqrt{2m_e k_B T_e} \frac{\partial v_e L}{\partial L} \quad (2)$$

374 where m_e is electron mass, plays a role equivalent to the effect of off-diagonal terms of the
 375 electron pressure tensor for anti-parallel reconnection and can cause the violation of the
 376 electron frozen-in condition at the X-point^{15,39}. The EMHD reconstruction has been
 377 successfully applied to EDR events in both the magnetopause⁴⁰ and magnetotail⁴¹ current
 378 layers.

379 Extended Data Fig. 2 shows the magnetic field, electron streamlines, and electric field
 380 reconstructed for the present ECS using the data from MMS 3, which was located near the
 381 centre of the MMS tetrahedron in the reconstruction plane. The final LMN axes were optimized
 382 by a multi-spacecraft method⁴⁰, which searches for the invariant-axis ($\hat{\mathbf{z}}_{\text{EMHD}}$) orientation that
 383 maximizes the correlation coefficient (Extended Data Fig. 2d) between the normalized
 384 components of the magnetic field and electron velocity measured by three spacecraft not used
 385 as input in the reconstruction and those predicted at points along the paths of the three
 386 spacecraft from the reconstructed field maps. The reconstruction axes thus determined are:
 387 $\hat{\mathbf{x}}_{\text{EMHD}} = (0.927, -0.271, 0.260)_{\text{GSM}}$, $\hat{\mathbf{y}}_{\text{EMHD}} = (-0.232, 0.131, 0.964)_{\text{GSM}}$ and $\hat{\mathbf{z}}_{\text{EMHD}} =$
 388 $(-0.296, -0.953, 0.059)_{\text{GSM}}$. Numerical errors may be large in regions away from the path
 389 ($y_{\text{EMHD}} = 0$) of MMS 3, especially near the four corners of the reconstruction domain. The
 390 reconstructed streamlines (Extended Data Fig. 2b) do not clearly show the inflow and outflow
 391 patterns as expected for steady reconnection but have a complex feature, probably because of
 392 time dependence associated with the growing magnetic island (Fig. 3). However, a quadrupolar
 393 pattern of $B_{z,\text{EMHD}} = -B_M$ related to the Hall effect^{42,43} is roughly reconstructed.

394 Extended Data Fig. 2d shows that the magnetic field is well reconstructed with a very high
 395 correlation coefficient; we can rely on the reconstructed magnetic fields (Fig. 3a–d). The small
 396 E_{Rec} (Fig. 4) also indicates that the time evolution associated with the island growth was slow,
 397 assuring that the assumption of time-independence was approximately satisfied.

398

399 **Polynomial reconstruction.**

400 The polynomial reconstruction^{13,44} recovers 3-D magnetic fields in and around the
 401 tetrahedron formed by the four spacecraft from instantaneous measurements by the four
 402 spacecraft of the magnetic field and particle current density. Several versions¹³ exist but all are
 403 based on second- or third-order Taylor expansion of the magnetic field. It produces a 3-D
 404 magnetic field for every moment during a selected time interval, and does not require any
 405 assumptions about structural dimensionality, time dependence, and frame velocity. Thus, it is
 406 complementary to the physics-based EMHD reconstruction in which steady and 2-D structures
 407 are assumed, so that the fields reconstructed using data from a finite time interval, which may
 408 violate the model assumptions, may well be time-aliased, while a larger reconstruction domain
 409 is allowed.

410 In this study, we used the 3-D reduced quadratic (RQ-3D) model¹³ in which less significant
 411 parts of the quadratic terms and higher-order terms are neglected. For 3-D fields, the calculation
 412 of magnetic flux inside a magnetic island (Fig. 4) is not trivial. The in-plane flux was calculated
 413 in two ways, one that first integrates B_N from $(L, N) = (L_X, N_X)$ to (L_O, N_X) and then adds B_L
 414 integrated from (L_O, N_X) to (L_O, N_O) , and the other that first integrates B_L from $(L, N) =$
 415 (L_X, N_X) to (L_X, N_O) and then adds B_N integrated from (L_X, N_O) to (L_O, N_O) , in the L - N plane

416 where the barycentre of the MMS tetrahedron is located. Here, $(L, N) = (L_X, N_X)$ is the
 417 location of the X-point and (L_O, N_O) of the O-point. The two flux values agree very well with
 418 each other, which corroborates the validity of the 2-D assumption made in the EMHD
 419 reconstruction.

420

421 **Magnetic-field annihilation due to off-diagonal terms of electron pressure tensor.**

422 It can be demonstrated that magnetic-field annihilation may occur across N in part extended
 423 in the L direction of an ECS with $\partial/\partial M = 0$, when the generalized Ohm's law is expressed by
 424 equation (1)

$$425 \quad \mathbf{E} = -\mathbf{v}_e \times \mathbf{B} + \frac{f(L, N)}{n_e e} \mathbf{M}.$$

426 We consider Faraday's law in the LMN coordinate system,

$$427 \quad \frac{\partial \mathbf{B}}{\partial t} = -\nabla \times \mathbf{E} = \nabla \times (\mathbf{v}_e \times \mathbf{B}) - \frac{1}{n_e e} \nabla f(L, N) \times \mathbf{M}. \quad (3)$$

428 Here we discuss only the contribution of the second term on the right-hand side (RHS) of
 429 equation (3), because the first term does not violate the electron frozen-in condition.
 430 Furthermore, only the L component

$$431 \quad \frac{\partial B_L}{\partial t} \approx \frac{1}{n_e e} \frac{\partial f(L, N)}{\partial N}$$

432 is considered, because $B_N \approx 0$ in ECSs elongated in the L direction. Since constant electron
 433 density, namely incompressible electron fluid ($\nabla \cdot \mathbf{v}_e = \partial v_{eL}/\partial L + \partial v_{eN}/\partial N = 0$), can be
 434 assumed in ECSs^{12,15}, the following relation results using equation (2)

$$435 \quad \frac{\partial B_L}{\partial t} \approx -\frac{\sqrt{2m_e k_B T_e}}{e} \frac{\partial^2 v_{eN}}{\partial N^2}.$$

436 We note that a relation $-B_\infty v_{eN} \approx B_L V_\infty$ is approximately satisfied inside an EDR because the
 437 spatial variations along N of B_L and v_{eN} would be very similar to each other with only sign
 438 difference (Extended Data Fig. 3c), while in the inflow region outside of the EDR $B_L v_{eN} \approx$
 439 $E_0 = B_\infty V_\infty$ holds for quasi-steady 2-D reconnection⁴⁵. Here E_0 is the reconnection electric
 440 field, and B_∞ and V_∞ are the B_L intensity and the electron inflow speed, respectively,
 441 immediately outside of the EDR, with $V_\infty \approx 0.1 V_{eA}$ for fast reconnection where the electron
 442 Alfvén speed $V_{eA} = B_\infty / (\mu_0 m_e n_e)^{1/2}$. Thus, the above relation becomes a diffusion equation
 443 for B_L

$$444 \quad \frac{\partial B_L}{\partial t} \approx D_B \frac{\partial^2 B_L}{\partial N^2}, \quad (4)$$

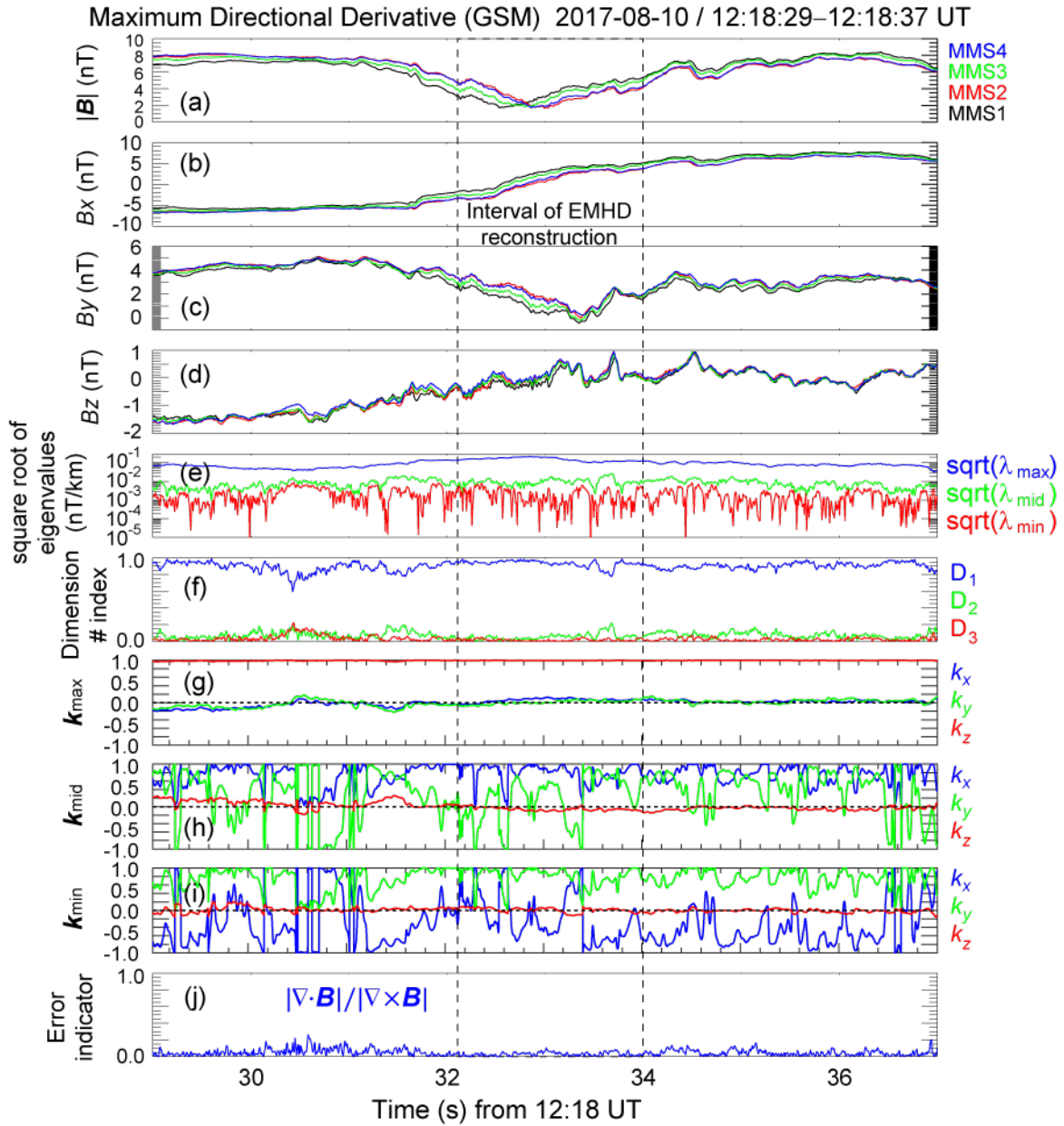
445 where the diffusion coefficient $D_B = r_{ge} V_\infty$ with the electron gyroradius $r_{ge} =$
 446 $(2m_e k_B T_e)^{1/2} / (e B_\infty)$. We can therefore conclude that in the presence of the term (2),
 447 equivalent to the non-gyrotropic electron pressure tensor term, the in-plane magnetic-field
 448 component B_L may be annihilated in an EDR. This conclusion is consistent with the theoretical
 449 analysis²¹ in which the term (2) was derived by discussing a diffusion of the electron current
 450 density j_{eM} that implies the annihilation of B_L . On the other hand, since the second term on the
 451 RHS of equation (3) has no M component, no annihilation of B_M (Hall magnetic field) occurs
 452 for 2-D reconnection. Moreover, the form of D_B indicates that in principle fast magnetic-field
 453 annihilation may occur when fast inflow of the in-plane magnetic flux exists. Notably, an
 454 experimental estimate of the diffusion coefficient $D \approx \delta V_\infty = d_e E_{str, M} / B_\infty \sim 10^{10} \text{ m}^2 \text{ s}^{-1}$ for
 455 the observed ECS with a thickness $\delta \approx d_e$ and electron beta $\beta_e = r_{ge}^2 / d_e^2 \sim 5$ is comparable
 456 to D_B . An exact solution of the EMHD equations with the dissipation term (2) (Extended Data
 457 Fig. 3), for which the inflowing B_L is all annihilated rather than reconnected in the EDR, was
 458 used in a benchmark test of the EMHD reconstruction code¹².

459

460 **Code availability.** All code used to analyse the MMS data in this study is based on the publicly

- 461 available SPEDAS tools⁴⁶ (<http://spedas.org/blog/>), except for the Matlab code for the EMHD
 462 and polynomial reconstructions. The Matlab code for the EMHD reconstruction can be found
 463 at the Zenodo (<https://doi.org/10.5281/zenodo.3900642>), and that for the polynomial
 464 reconstruction at <https://doi.org/10.5281/zenodo.3906853>.
- 465 **Data availability.** All MMS data used in this study are publicly available via the MMS Science
 466 Data Center at <https://lasp.colorado.edu/mms/sdc/public/>. Geomagnetic Auroral Electrojet
 467 index is available at <http://wdc.kugi.kyoto-u.ac.jp/aedir/>.
- 468
- 469 29. Torbert, R. B. et al. The FIELDS instrument suite on MMS: scientific objectives,
 470 measurements, and data products. *Space Sci. Rev.* **199**, 105–135 (2016).
 - 471 30. Lindqvist, P.-A., Olsson, G., Torbert, R. B. et al. The Spin-plane Double Probe electric
 472 field instrument for MMS, *Space Sci. Rev.*, **199**, 137–165 (2016).
 - 473 31. Ergun, R. E., Tucker, S., Westfall, J. et al. The axial double probe and fields signal
 474 processing for the MMS mission, *Space Sci. Rev.*, **199**, 167–188 (2016).
 - 475 32. Russell, C. T., Anderson, B. J., Baumjohann, W. et al. The Magnetospheric Multiscale
 476 Magnetometers, *Space Sci. Rev.*, **199**, 189–256 (2016).
 - 477 33. Pollock, C. et al. Fast plasma investigation for Magnetospheric Multiscale. *Space Sci. Rev.*
 478 **199**, 331–406 (2016).
 - 479 34. Denton, R. E., Sonnerup, B. U. Ö., Russell, C. T. et al. Determining L-M-N current sheet
 480 coordinates at the magnetopause from Magnetospheric Multiscale data. *J. Geophys. Res.*
 481 *Space Physics*, **123**, 2274–2295 (2018).
 - 482 35. Sonnerup, B. U. Ö. & Scheible, M. in *Analysis Methods for Multi-Spacecraft Data* (eds
 483 Paschmann, G. & Daly, P. W.) Ch. 8, 185–220 (ISSI/ESA, 1998).
 - 484 36. Shi, Q. Q., Tian, A. M., Bai, S. C. et al. Dimensionality, coordinate system and reference
 485 frame for analysis of in-situ space plasma and field data. *Space Sci. Rev.*, **215**, 35 (2019).
 - 486 37. Shi, Q. Q., Shen, C., Dunlop, M. W. et al. Motion of observed structures calculated from
 487 multi-point magnetic field measurements: Application to Cluster. *Geophys. Res. Lett.*, **33**,
 488 L08109 (2006).
 - 489 38. Denton, R. E., Sonnerup, B. U. Ö., Hasegawa, H. et al. Motion of the MMS spacecraft
 490 relative to the magnetic reconnection structure observed on 16 Oct 2015 at 1307 UT.
 491 *Geophys. Res. Lett.*, **43**, 5589–5596 (2016).
 - 492 39. Kuznetsova, M. M., Hesse, M., Rastaetter, L. et al. Multiscale modeling of magnetospheric
 493 reconnection, *J. Geophys. Res.*, **112**, A10210 (2007).
 - 494 40. Hasegawa, H., Sonnerup, B. U. Ö., Denton, R. E. et al. Reconstruction of the electron
 495 diffusion region observed by the Magnetospheric Multiscale spacecraft: First results.
 496 *Geophys. Res. Lett.*, **44**, 4566–4574 (2017).
 - 497 41. Hasegawa, H., Denton, R. E., Nakamura, R. et al. Reconstruction of the electron diffusion
 498 region of magnetotail reconnection seen by the MMS spacecraft on 11 July 2017. *J.*
 499 *Geophys. Res. Space Physics*, **124**, 122–138 (2019).
 - 500 42. Nagai, T., Shinohara, I., Fujimoto, M. et al. Geotail observations of the Hall current system:
 501 Evidence of magnetic reconnection in the magnetotail. *J. Geophys. Res.*, **106**, 25929–25949
 502 (2001).
 - 503 43. Øieroset, M., Phan, T. D., Fujimoto, M., Lin, R. P., & Lepping, R. P. In situ detection of
 504 collisionless reconnection in the Earth’s magnetotail. *Nature*, **412**, 414–417 (2001).
 - 505 44. Torbert, R. B., Dors, I., Argall, M. R. et al. A new method of 3-D magnetic field
 506 reconstruction. *Geophys. Res. Lett.*, **47**, e2019GL085542 (2020).
 - 507 45. Liu, Y.-H., Hesse, M., Guo, F. et al. Why does steady-state magnetic reconnection have a
 508 maximum local rate of order 0.1? *Phys. Rev. Lett.*, **118**, 085101 (2017).
 - 509 46. Angelopoulos, V., Cruce, P., Drozdov, A., Grimes, E. W. et al. The Space Physics
 510 Environment Data Analysis System (SPEDAS). *Space Sci. Rev.*, **215**, 9 (2019).

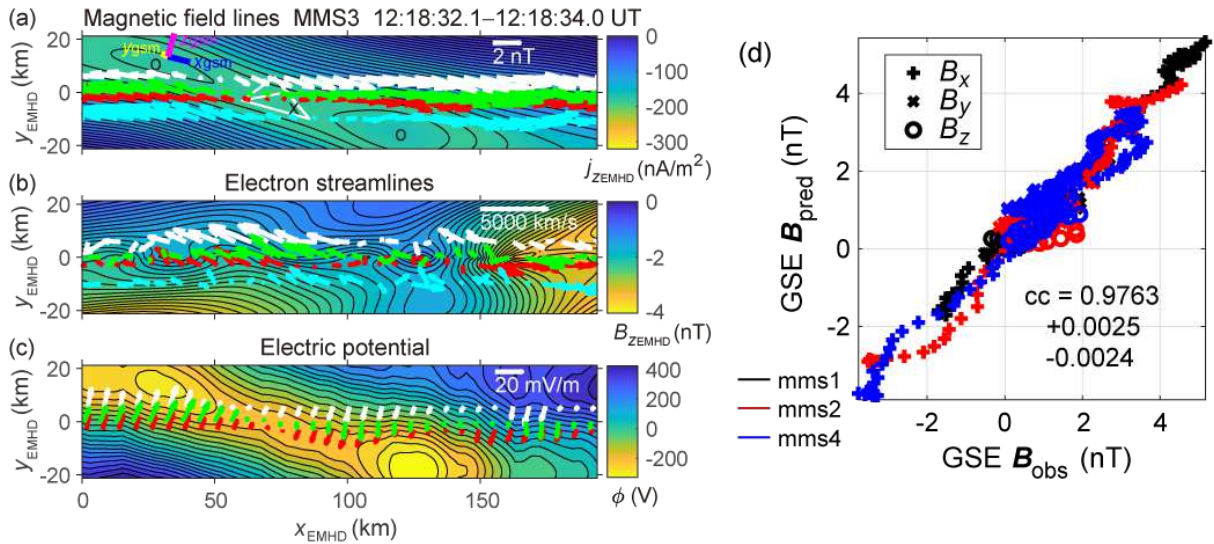
- 511 47. Rezeau, L., Belmont, G., Manuzzo, R., Aunai, N. & Dargent, J. Analyzing the
512 magnetopause internal structure: New possibilities offered by MMS tested in a case study.
513 *J. Geophys. Res. Space Physics*, **123**, 227–241 (2018).
514 48. Kawano, H. & Higuchi, T. The bootstrap method in space physics: Error estimation for
515 minimum variance analysis. *Geophys. Res. Lett.*, **22**, 307–310 (1995).



516

517 **Extended Data Fig. 1 | Results from the MDD method³⁶ applied to an interval 12:18:29–**
 518 **12:18:37 UT. a–d, GSM components of the magnetic field measured by the four MMS**
 519 **spacecraft (a; $|\mathbf{B}|$, b; B_x , c; B_y , d; B_z). e, Eigenvalues (λ_{\max} , λ_{mid} , λ_{\min}) of the 3×3 MDD**
 520 **matrix³⁶. f, Dimension number indices⁴⁷, defined as $D_1 = (\lambda_{\max} - \lambda_{\text{mid}})/\lambda_{\max}$, $D_2 =$**
 521 **$(\lambda_{\text{mid}} - \lambda_{\min})/\lambda_{\max}$, and $D_3 = \lambda_{\min}/\lambda_{\max}$, that can be used as measures of the dimensionality**
 522 **of the structure encountered by the spacecraft, . g–i, Eigenvectors corresponding to the three**
 523 **eigenvalues (g; \mathbf{k}_{\max} , h; \mathbf{k}_{mid} , i; \mathbf{k}_{\min}). j, $|\nabla \cdot \mathbf{B}|/|\nabla \times \mathbf{B}|$ as an error proxy.**

524



525

526

527

528

529

530

531

532

533

534

535

536

537

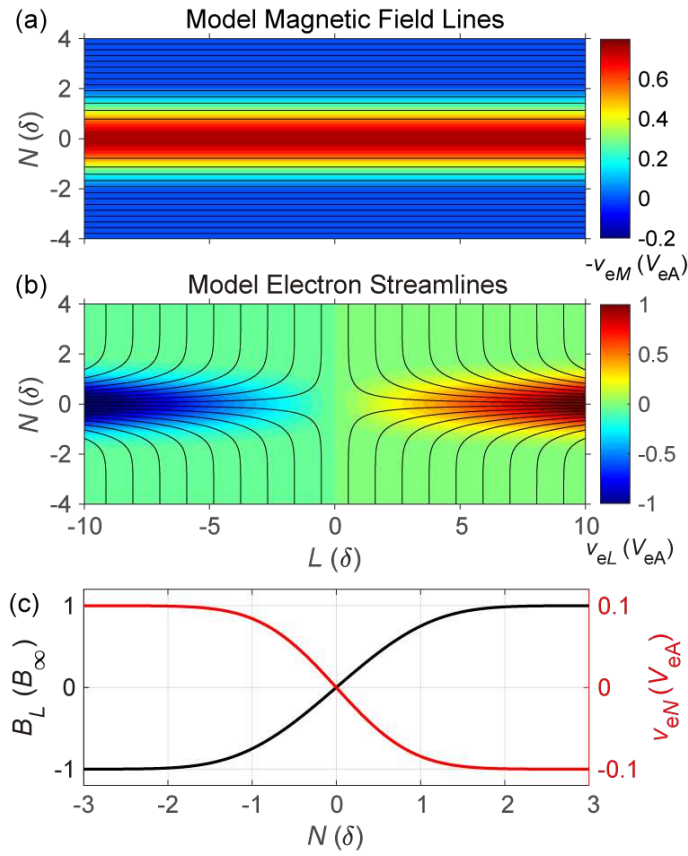
538

539

540

Extended Data Fig. 2 | 2-D magnetic, electrostatic and electron-velocity fields recovered from the EMHD reconstruction applied to the MMS 3 data at 12:18:32.1–12:18:34.0 UT.

a, Reconstructed in-plane magnetic field-lines with the out-of-plane component ($j_{z,EMHD}$) of the reconstructed current density in colour. Arrows show the projections onto the reconstruction plane of the measured magnetic fields (white, MMS 1; red, MMS 2; green, MMS 3; cyan, MMS 4) along the paths ($y_{EMHD} = \text{const.}$) of the four spacecraft. **b**, Reconstructed electron streamlines with the out-of-plane component ($B_{z,EMHD}$) of the reconstructed magnetic field in colour. Arrows show the projections of the measured electron velocities transformed into the structure-rest frame. **c**, Reconstructed electrostatic potential (ϕ), along with the projections of the measured electric fields ($\mathbf{E}_{str} = \mathbf{E} + \mathbf{V}_{str} \times \mathbf{B}$) transformed into the structure-rest frame. **d**, Correlation between the components in geocentric solar ecliptic (GSE) coordinates of the measured magnetic field (B_x : plus, B_y : cross, and B_z : circle) and those predicted from the reconstruction along the paths of MMS 1 (black), MMS 2 (red), and MMS 4 (blue) not used as input for the reconstruction. The confidence intervals of the correlation coefficients corresponding to ± 1 sigma were estimated by the bootstrap method⁴⁸.



541

542 **Extended Data Fig. 3 | Exact solution of the dissipative EMHD equations¹² showing the**
 543 **magnetic field and electron velocity profiles in and around an ECS with a thickness (δ)**
 544 **comparable to d_e .** **a**, Magnetic field-lines in the L - N plane with the out-of-plane ($-M$)
 545 component of the electron velocity in unit of V_{eA} in colour. **b**, Electron streamlines with the L
 546 component (v_{eL}) of the electron velocity in colour. **c**, Spatial profiles along N of v_{eN} and B_L in
 547 unit of the field intensity (B_∞) outside of the ECS.

Figures

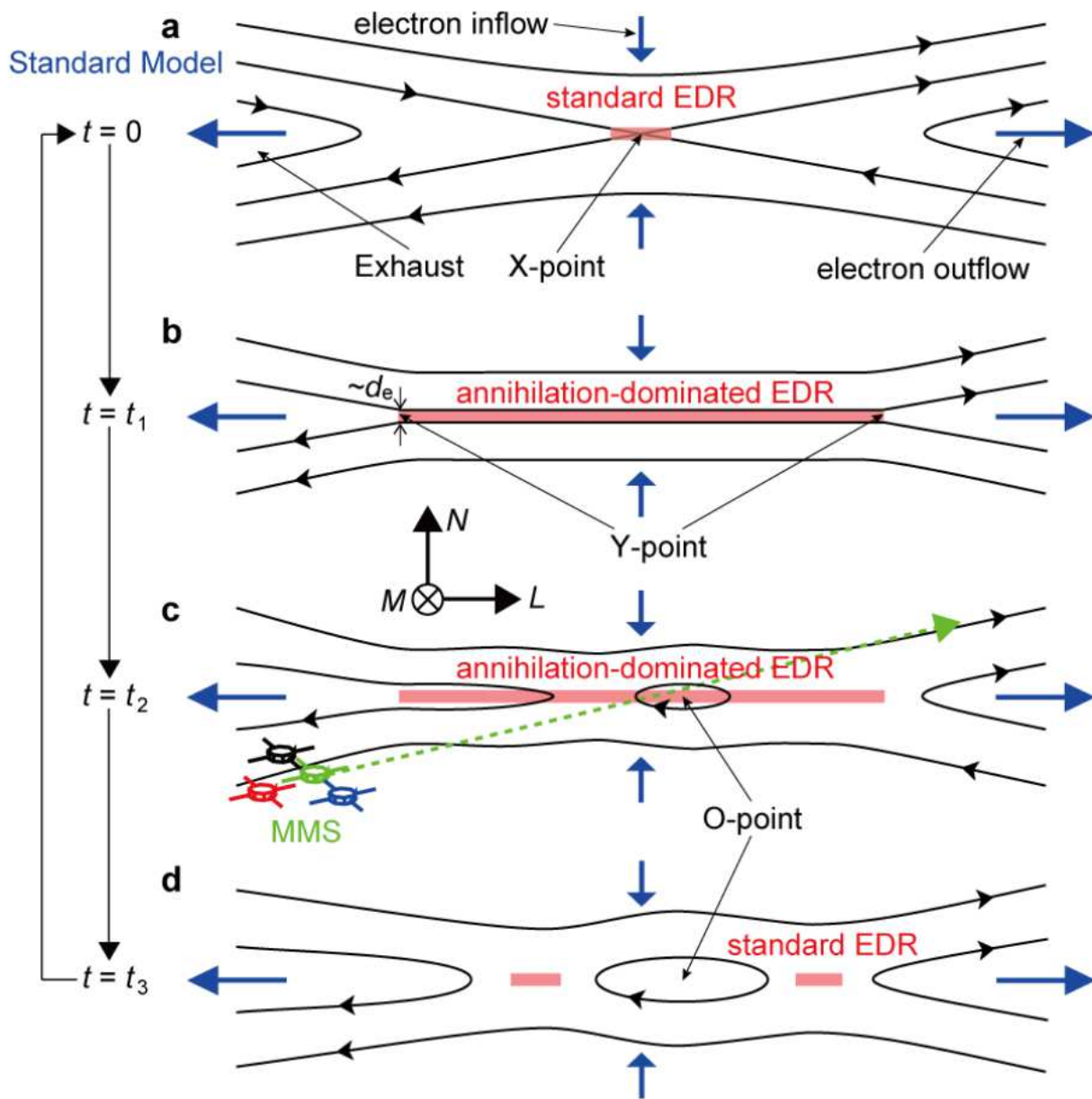


Figure 1

Standard picture of the reconnection region and possible sequence of time evolution of the observed electron-scale current sheet. a, Standard EDR with an X-type magnetic-field geometry where the magnetic-to-particle energy conversion is mostly due to reconnection⁴. b, EDR after elongation along L, as seen in simulation⁷, where the energy conversion may be mostly due to magnetic-field annihilation (Methods). c, Initial stage of the magnetic-island formation in the EDR, as observed by MMS. d, Possible later stage of the island growth in exhausts of the EDRs where the energy conversion is again dominated by reconnection.

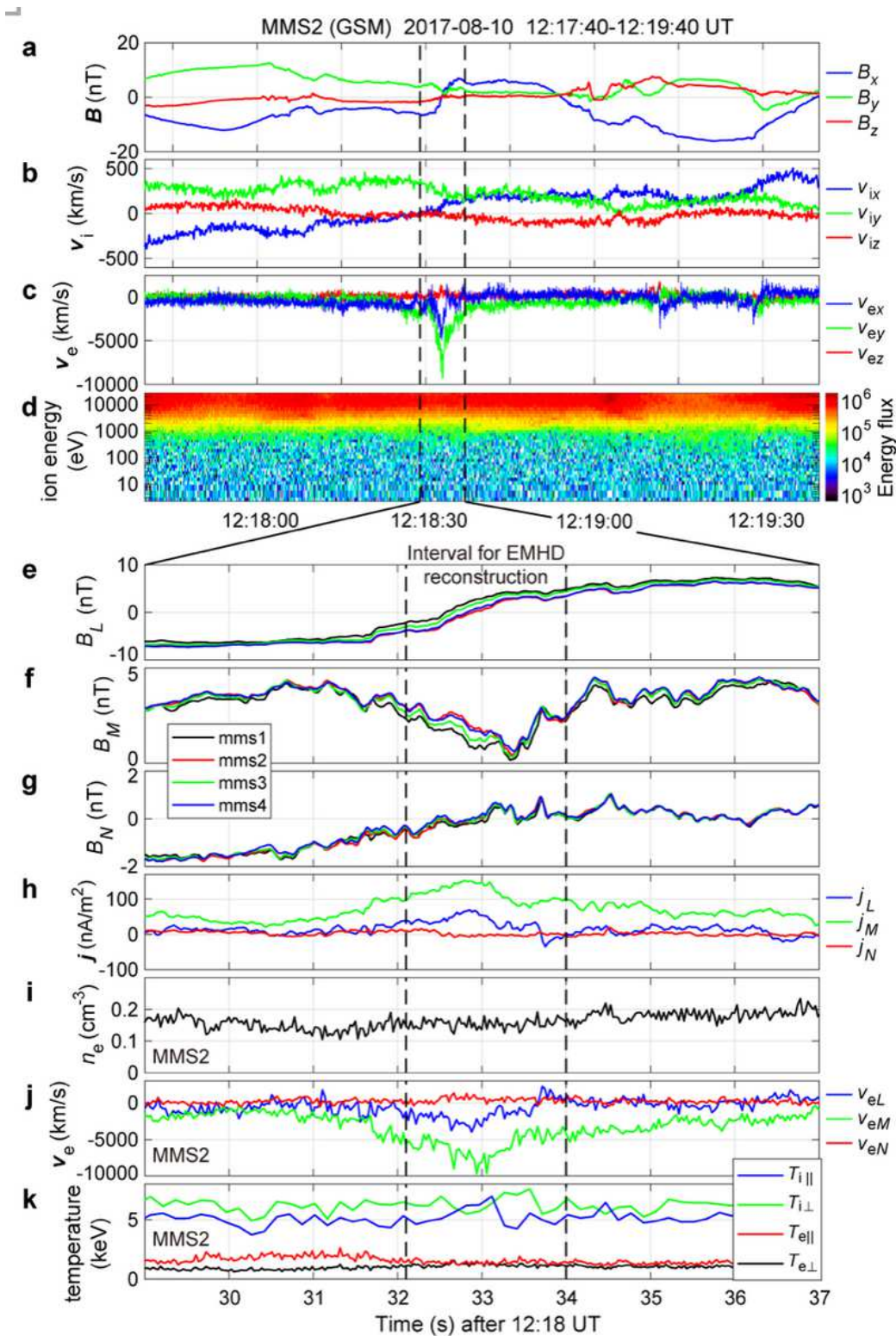


Figure 2

Overview of MMS observations of an ECS with both ion and electron reconnection jet signatures. a–d, GSM components of the magnetic field (a; B_x , B_y and B_z), ion velocity (b; v_{ix} , v_{iy} and v_{iz}), electron velocity (c; v_{ex} , v_{ey} and v_{ez}) and ion energy-time spectrogram of omni-directional differential energy flux (d; colour scale, in units of $\text{keV s}^{-1} \text{cm}^{-2} \text{sr}^{-1} \text{keV}^{-1}$) seen by MMS 2. e–h, Components in a common current-sheet (LMN) coordinate system of the magnetic field (e–g; B_L , B_M and B_N) from all four

spacecraft (black, MMS 1; red, MMS 2; green, MMS 3; blue, MMS 4) and current density $j = (\nabla \times B) / \mu_0$ (h; j_L , j_M and j_N). i–k, MMS 2 measurements of the electron density (i; n_e), electron velocity in LMN coordinates (j; v_{eL} , v_{eM} and v_{eN}), and ion and electron temperatures (k; T_i and T_e) in the directions parallel (\parallel) and perpendicular (\perp) to the local magnetic field.

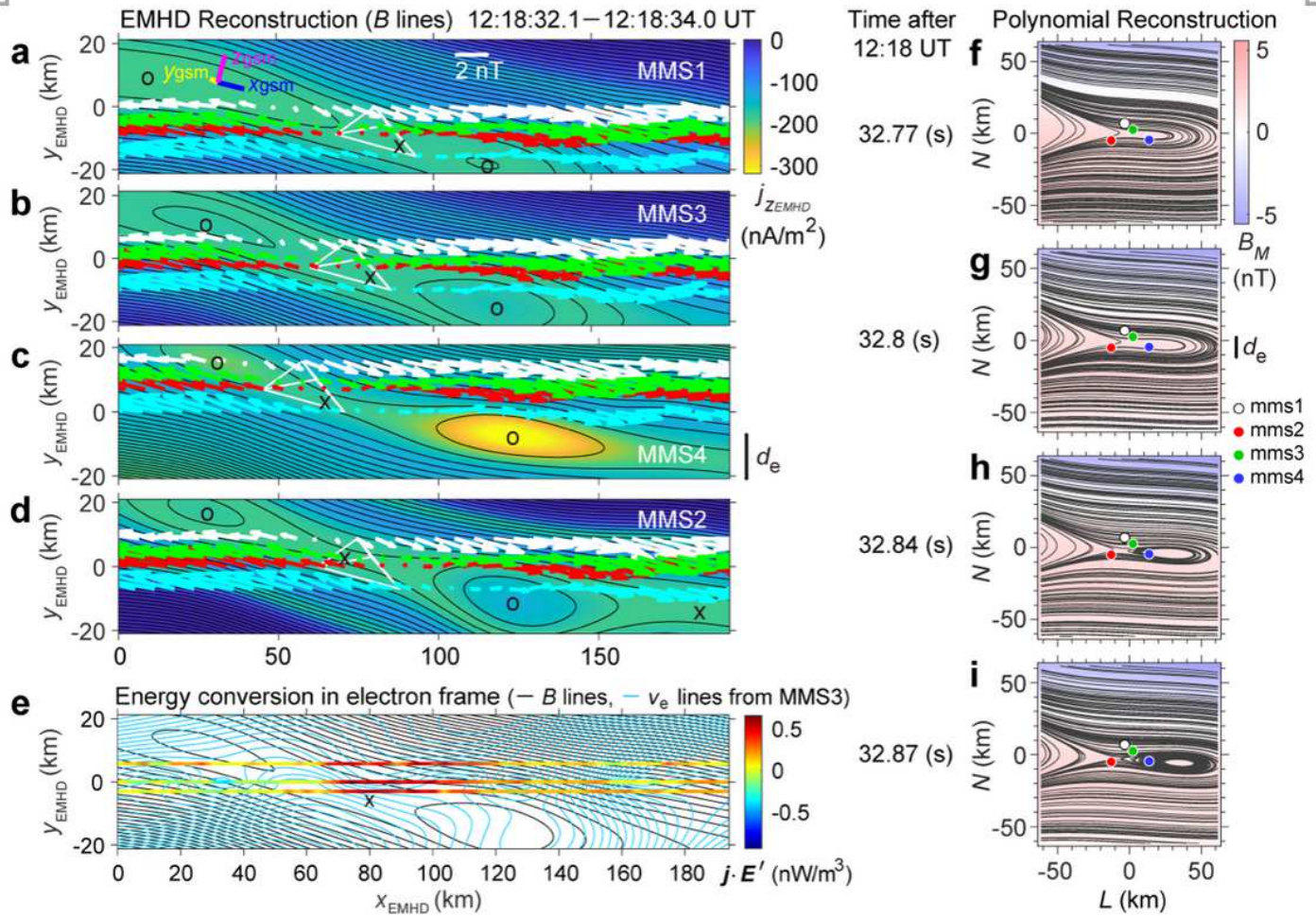


Figure 3

Magnetic fields recovered from the two reconstruction methods (Methods). a–d, 2-D magnetic fields from the EMHD reconstruction using the data taken at 12:18:32.1–12:18:34.0 UT individually for each of the four spacecraft, shown in the order of current sheet crossing (MMS 1, a; MMS 3, b; MMS 4, c; then MMS 2, d; as seen in Fig. 2e). Black curves show the reconstructed magnetic field-lines, colours the out-of-plane component ($j_z, EMHD$) of the reconstructed current density, and arrows the projections onto the reconstruction ($x_{EMHD}-y_{EMHD}$) plane of the measured magnetic fields (white, MMS 1; red, MMS 2; green, MMS 3; cyan, MMS 4) along the paths of the four spacecraft. The bars near the upper-left corner of Fig. 3a are the projections of the unit GSM axes (blue, $x \parallel GSM$; yellow, $y \parallel GSM$; magenta, $z \parallel GSM$). e, Magnetic field-lines (black curves) and electron streamlines (blue curves) reconstructed from the MMS 3 data, with $j \cdot E' = j_p \cdot (E + v_e \times B)$ measured along the paths of MMS 1, MMS 2, and MMS 3 in colour. f–i, Projection onto the L–N plane of 3-D magnetic field-lines reconstructed using the polynomial

reconstruction13 from instantaneous measurements (time after 12:18 UT: 32.77 s, f; 32.8 s, g; 32.84 s, h; 32.87 s, i) by the four spacecraft of B and jp, with reconstructed BM in colour.

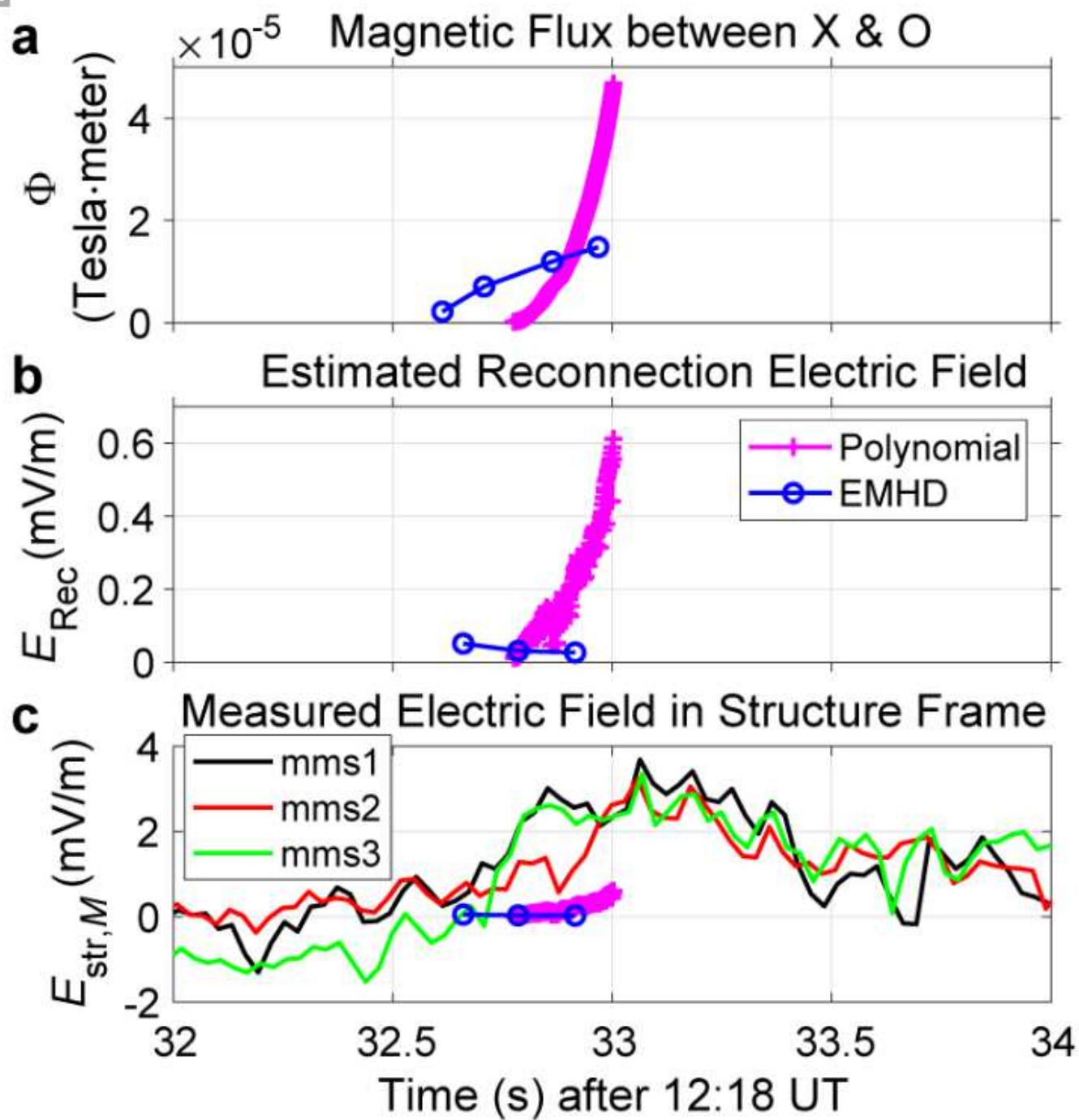


Figure 4

Reconnection electric fields, estimated from the EMHD and polynomial reconstructions, compared with the measured electric field. a, In-plane magnetic flux (Φ) embedded between the X- and O-points around the centre of the reconstruction domain as a function of time which is defined as that of the current sheet crossing ($BL=0$) for the EMHD reconstruction. b, Reconnection electric field ($E_{Rec}=\partial\Phi/\partial t$) estimated from the temporal rate of change in Φ . c, M component ($E_{str,M}$) of the electric field from MMS 1, MMS 2, and

MMS 3 that made reliable electric field measurements, transformed into the frame comoving with the structure (Methods), along with ERec.